RISK ASSESSMENT METHOD FOR BACK-REFLECTIONS FROM SPACE DEBRIS IN HIGH-POWER LASER RANGING

Stefan Scharring, Jürgen Kästel, Thomas Klumpp, Nils Bartels, Wolfgang Riede, Jochen Speiser

German Aerospace Centre (DLR), Institute of Technical Physics, Pfaffenwaldring 38-40, 70569 Stuttgart, Germany, Email: stefan.scharring@dlr.de

ABSTRACT

A versatile method to assess the risk arising from pulsed laser radiation reflected from space debris is presented which is based on the thresholds of maximum permissible exposure (MPE) to laser irradiation as they apply by European legislation. Gaussian beam propagation is employed considering atmospheric attenuation and turbulence-induced beam broadening. For the reflected beam specular reflection is considered as a worst-case estimate, comprising effects of target outshining and diffraction.

System-specific risk charts are derived to assess the amount by which the MPE value might be exceeded for downlink reflections. These charts are directly connected to the orbital and rotational motion of the debris object via the resulting glint motion and size which is determined by the overpass geometry.

1 INTRODUCTION

Laser-based tracking and ranging is a well-established method for precise orbit determination. While in the cooperative case retroreflectors on board the targeted satellite allow for laser ranging operations at comparably low laser power, space debris demands for significantly higher power levels. In terms of laser safety, specific attention is paid to deconflict with air traffic [1]. By either temporarily shutting down laser operation or establishing a sufficiently large no-fly zone, the risk attached to laser irradiation of the human eye (or skin) exceeding the applicable maximum permissible exposure (MPE) can be suppressed.

While risks arising from laser radiation in the uplink can be ruled out this way, possible risks arising from reflected laser light in the downlink are usually disregarded due to the simple fact that debris laser ranging deals with photon counting rather than with issues from detector overexposure. Nevertheless, the progressing availability of pulsed lasers with increasing average power, the necessity of orbital data for even very small debris objects as well as advances in turbulence compensation by adaptive optics justify a thorough assessment of the risk from reflected laser radiation, cf. Fig. 1.

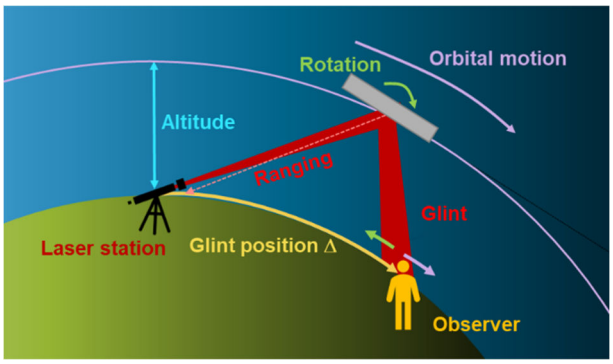

Figure 1. Illustration of potential irradiation risks from specular reflections ("glints") in laser ranging: Glint size and energy are determined by beam divergence, reflecting surface properties, and diffraction, while the exposure duration can be derived from orbital motion and object rotation.

2 LASER BEAM EXPOSURE LIMITS

Lasers emit coherent light, which means that the outgoing photons are nearly identical regarding their wavelength, phase, and direction. For that reason, laser beams can be focused to a very small spot in which the light intensity is relatively high compared to the much larger spot which would be generated from focusing an incoherent light beam with the same photon flux.

Image generation in the human eye relies on focusing of incoming light by cornea and lens to the photoreceptor cells of the retina from where visual perception is induced by sending nerve impulses to the visual cortex of the human brain. At high thermal loads, stemming from large light intensities, retina cells can be irreversibly damaged yielding a permanently black area in the respective solid angle of the field of vision. High light intensities, and thus, a source of transient dazzling or potential injury, can easily be generated by focusing a laser beam of even relatively low intensity stemming from, e.g., a laser pointer. Therefore, thresholds for the maximum permissible exposure (MPE) to laser radiation have commonly been agreed upon and legally set in force which apply for any kind of laser operation.

Damage to human health by laser radiation cannot only be generated to the eye's retina, but unfocused laser of greater intensities can adversely impact to other parts of the human eye, namely cornea, lens, and vitreous body,

and, beyond that, even to human skin as well. Since those tissues differ greatly from each other in their composition and thermo-optical material properties, MPE thresholds depend strongly on target (eye or skin), laser wavelength λ, and various irradiation conditions, e.g., its duration t_L and – for pulsed lasers – as well on pulse duration τ and the number N_p of laser pulses.

Legally binding MPE limits can differ with respect to national jurisdiction, hence, for the sake of simplicity, in the following we restrain our considerations to the regulations applicable within the European Union [2] at the time of writing. However, our simulation results serve for orientation purposes only and no legal liability is taken regarding harm from any practical application of our findings in a real-world scenario. Instead, in any case a dedicated laser safety officer is foreseen by law for risk assessment of the specific application. Here, we hope that our study may serve as a tool to facilitate the analysis of the rather complex interaction dynamics of laser ranging.

2.1 Single Pulse

In order to obtain high photon returns from the orbital target, ranging lasers are usually operated in the visible (VIS) and near-infrared (NIR) part of the spectrum of electromagnetic waves, since losses from atmospheric attenuation are typically low and the short wavelength yields a narrow beam cone. In particular, considerably high laser power can be obtained from commercially available Nd:YAG (Neodymium-doped Yttrium Aluminum Garnet) lasers emitting at λ = 1064 nm and, frequency-doubled, 532 nm, respectively. Such lasers are widely used, e.g., within the International Laser Ranging Service (ILRS) [3].

Table 1. Laser parameters of selected systems for satellite laser ranging (SLR): ILRS Station Code, Wavelength λ, pulse duration τ, pulse energy E_L, pulse repetition rate $f_{rep.}$, transmitter aperture D_T, and beam quality parameter M^2.

ID[1]	λ [nm]	τ [ps]	E_L [mJ]	f_{rep} [Hz]	D_T [cm]	M^2 [-]
GEOL	532	9	15	60	100	n.d.
GRZL	532	10	0.4	2000	7	1.15
UROL	1062	1E4	0.05	1E5	10	1.5
SMIL	1064	500	0.085	5E4	10	1.5

[1] Station codes and data references: GEOL: Geochang [4], GRZL: Graz [5], UROL: UFO Stuttgart (decommissioned), [6], SMIL: mini-SLR Stuttgart [7]

Depending on the desired range resolution and photon return flux, pulse durations range from a few picoseconds up to almost hundred nanoseconds while the average laser power is typically between slightly below 1W up to tens of Watt, cf. Tab. 1 and Tab. 2. Suitable powerful solid-state lasers (SSL) with different laser media exist exhibiting more or less deviating wavelengths. Currently, the usage of larger wavelengths, e.g., λ = 1645 nm, for so-called "eye-safe" laser ranging is under research in order to operate at high laser power in an optical regime where MPE limits are relatively large as well [8,9], cf. Fig. 2.

Table 2. Laser parameters of selected systems for space debris laser ranging (SDLR): Wavelength λ, pulse duration τ, pulse energy E_L, pulse repetition rate $f_{rep,}$ transmitter aperture D_T, and beam quality parameter M^2.

ID[1]	λ [nm]	τ [ns]	E_L [mJ]	f_{rep} [Hz]	D_T [cm]	M^2 [-]
GEOL	532	4-8	2500	10	100	n.d.
SHA2	532	10	2000	20	21	n.d.
BORL	532	3-5	450	10	65	n.d.
GRZL	532	3	80	200	7	1.43[2]
GRZL[3]	532	0.01	0.017	1E6	7	1.15
JKO	1064	10	50	1000	10	1.5
JKO2	1645	75	17.5	1000	10	1.5

[1]GEOL, GRZL: see above, SHA2: Shanghai [10], BORL: Borowiec [11] JKO: Johannes-Kepler-Observatory DLR Empfingen (not an ILRS station) [12], JKO2: "eye-safe" configuration of JKO [9]; [2]derived from [13]; [3]also used for SLR.

The MPE for single laser pulses, denoted as $\Phi_{MPE,1}$, relates to the fluence Φ at an area perpendicular to the beam propagation axis while the irradiation time t_L is given by the pulse duration τ. Corresponding MPE limits can be taken from Fig. 2.

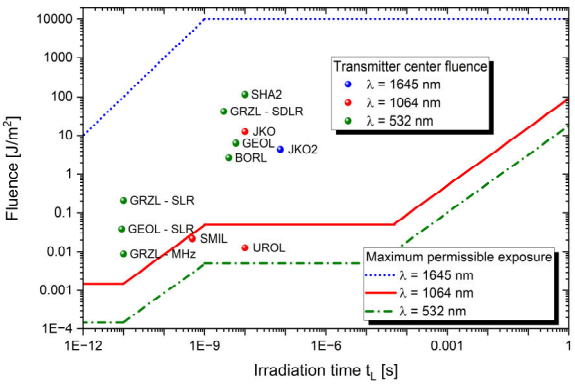

Figure 2. MPE for the human eye regarding pulsed laser radiation and fluence and the transmitter center for different ranging stations, cf. Tab. 1 and Tab. 2. Thermal correction, cf. Sec. 2.3, is not applied here.

As a general trend it can be seen that MPE values tend to decrease as the pulse length decreases which can be

attributed to the high laser intensity $I = \Phi/\tau$ at given Φ when τ is very short. Additionally, MPE values for $\lambda = 1645$ nm are on the order of four magnitudes higher than those of the other depicted wavelengths, highlighting the intended suitability for "eye-safe" laser ranging. The term "eye-safe" and the high MPE values stem from the fact that for wavelengths greater than 1400 nm, light is already absorbed at the eye's cornea, lens, and vitreous body, which strongly protects the retina being the only one of those eye components that cannot be fixed in a surgery after a laser incident.

2.2 Multiple Pulses

Ranging lasers can operate at high pulse repetition rates. Hence, it is well conceivable, that a significant number of subsequent laser pulses enters the human eye during an accidental irradiation. Therefore, two additional MPEs apply, i.e., the lowest one of all is decisive in a related irradiation scenario.

As secondary MPE threshold, the limit for pulse accumulation, $\Phi_{MPE,N}$, is given as a cumulative value. While its nominal value equals the one which is used for $\Phi_{MPE,1}$, the accumulated fluence, i.e., the sum of the fluences from all involved laser pulses, is referred to for MPE assessment. In turn, the irradiation time in Fig. 2 is given by the timespan t_L between the first and the last applicable laser pulse, cf. Sec. 4.2 for details.

2.3 Thermally Corrected Single Pulse

Finally, it has to be considered that the irradiated tissue might heat up during a series of subsequent laser pulses. Hence, the pre-heated material can easier be damaged by laser pulses at the end of the pulse train than by the initial pulse.

To account for this circumstance with repetitively pulsed irradiation, the tertiary MPE threshold again refers to a single laser pulse regarding its fluence and pulse length, however, at a reduced level acknowledging thermal pre-conditioning. Thus, the MPE for a thermally corrected single pulse is given by $\Phi_{MPE,T} = \Phi_{MPE,1} \times N_p^{-0.25}$. For very high repetition rates it has to be considered that pulses with a temporal spacing of less than 18 µs (for $\lambda = 532$ nm and 1030 nm) and 50 µs (for 1064 nm), respectively, are summarized to a single pulse. For $\lambda = 1645$ nm, the respective accumulation timespan amounts to 10 seconds and is not relevant in the following.

3 STATIC GLINT COMPUTATION

In order to quantify the fluence and criticality of a reflection glint on ground, we derive how the laser beam size and energy is affected by uplink and downlink transmission through the atmosphere and explore the impact of target reflectivity and size.

3.1 Laser Beam Propagation

For laser ranging operations, the expected average photon flux is usually estimated using Degnan's well-known link budget equation [14] which allows for the computation of glint size and energy with some generalizations. While the far field divergence of the laser system has to be assessed for that, in our study we chose to derive the evolution for the laser spot radius $w(z)$ as function of the distance z to the laser transmitter considering atmospheric turbulence using [15,16]

$$[w(z)]^2 = w_0^2 + \left(\frac{M^2 \lambda\, z}{\pi\, w_0}\right)^2 + 8\left(\frac{\lambda\, z}{\pi\, r_0}\right)^2 \left(1 - 0.26\sqrt[3]{\frac{r_0}{w_0}}\right)^2 \quad (1)$$

where the initial (Gaussian) beam radius w_0 is set to 35.75% of the transmitter aperture diameter D_T, which corresponds to a pulse energy loss of 2% due to outshining [17]. The second term of Eq. 1 describes the Gaussian beam propagation using the laser beam quality parameter M^2, whereas turbulence-induced beam broadening is represented by the third term comprising the spherical-wave coherence diameter r_0 in uplink, which is defined as [15,18]

$$r_0 = \left(0.42 \frac{4 \cdot \pi^2}{\lambda^2} \sec[\zeta]\, h \cdot c\right)^{-3/5} \quad (2)$$

where ζ is the beam pointing zenith angle, h is the orbit altitude of the target and c is given by

$$c = \int_0^1 d\xi (1-\xi)^{\frac{5}{3}} C_n^2(\xi h) \quad (3)$$

with the height-dependent turbulence strength C_n^2.

In our simulations, we use C_n^2 data from the HAP model (daytime) [57]. As turbulence is predominant at lower atmospheric layers and turbulence-induced beam broadening increases with distance behind the relevant layers, turbulence effects are only considered for uplink, but not in downlink.

Note that in Eq. 1, $w(z)$ denotes the short-term beam radius, whereas in the link budget equation the long-term beam radius is employed, since pointing jitter has to be included there for the assessment of the average photon flux. For risk analysis, however, we discard beam offset statistics for the sake of a worst-case assessment.

The total extinction $E(\zeta)$ of a laser beam traversing the atmosphere at a zenith angle ζ has been derived using

$$E(\zeta) = 1 - \exp\left(-\sec\zeta \int \gamma_e(h)\, dh\right) \quad (4a)$$

with

$$\int \gamma_e(h)\, dh = \begin{cases} 0.3942 & (\lambda = 515\, nm) \\ 0.1445 & (\lambda = 1060\, nm) \\ 0.1032 & (\lambda = 1536\, nm) \end{cases} \quad (4b)$$

which can be deduced by linear interpolation of the altitude-dependent data for atmospheric extinction $\gamma_e(h)$ tabulated in [20] for clear atmospheric conditions at medium geographical latitudes. In our simulations, we used the data from Eq. 4b for the wavelength closest to the one of the laser ranging system.

Other than with turbulence effects, atmospheric extinction has been considered both in uplink as well as in downlink. However, again to undertake a worst-case assessment, absorption from (slight) cloud cover is not considered here, whereas possible absorption by cirrus clouds is included in [14].

3.2 Reflection from a Space Object

The link budget equation originates from satellite laser ranging applications, where the usage of an on-board laser retroreflector is represented by a correspondingly large optical cross-section. However, such a cooperative kind of laser-target interaction cannot be assumed for laser ranging to space debris in general. Instead, the object's surface has to be considered, which reflects the incoming beam more or less diffusely exhibiting a less or more pronounced angular lobe indicating specular reflection, strongly dependent on the material's properties, in particular, its surface roughness.

In light curve analysis, sunlight reflections at a space object are modelled using surface-specific bidirectional reflectivity functions (BRDF) [21], which are a standard resource in computer graphics rendering. While the BRDF's definition to relate the reflected radiance L_o in a certain direction ω_o of reflection to the irradiance E_i from a given incidence direction ω_i using [22]

$$BRDF(\omega_i, \omega_o, \lambda) = \frac{dL_0(\omega_0, \omega_i, \lambda)}{dE(\omega_i, \lambda)} \quad (5)$$

constitutes a general description of both diffuse and specular light reflection, the related surface-specific BRDF data has to be seen in the context of irradiation conditions: Typically, such data is obtained under incoherent illumination [23] being the most prevalent irradiation condition. Moreover, related models attempting to derive BRDF data directly from surface parameters like reflectivity and roughness, frequently rely on, e.g., microfacet theory assuming ray optics [24], which is not appropriate for laser irradiation since its coherence has to be considered in diffraction effects using wave optics.

BRDF models which involve wave optics considerations turn out to be significantly more complex than those based on geometrical optics. Nevertheless, they offer advantages regarding the simulation of wavelength-dependencies, which is helpful in hyperspectral remote sensing [25]. Moreover, experimental BRDF data from scratched surfaces underline the reasonability to consider diffraction in modelling [26]. In particular, laser speckles can be described by superimposing glints from small-scale surfaces in a wave optics model [27].

Beyond the mentioned laser scattering we observed in own experimental work that when laser light is reflected at a large target with significant surface roughness, a fraction of the beam can still be modelled using Gaussian beam propagation behind the irradiated target [28], i.e., following Eq. 1 (without turbulence term). As this is a macro-scale phenomenon involving the radius of the outgoing beam, it cannot be captured in a purely material-specific BRDF. However, in analogy to the considerations in [26], it is conceivable that a *target-specific* BRDF can reasonably be defined in the far field of the reflected beam.

The portion of laser radiation which is unaffected by surface irregularities in reflection certainly depends on surface roughness parameters, but the related specific dependencies still remain unclear. For that reason, to cut a long story short, we discard any BRDF data and model the space object as a perfectly flat surface and, in order to derive a worst-case assessment, assume 100% reflectivity.

While this assumption surely overestimates the glint intensity on ground, one would otherwise run the risk to strongly underestimate it by using BRDF data for space materials, as, e.g., from [29], discarding a potentially harmful glint of only a few µrad beam divergence from partially undisturbed specular reflection.

3.3 Laser Beam Diffraction

To facilitate the subsequent computations, we represent the target by a circular, flat, and perfectly reflecting disk with the diameter d_{cs}. If the surface normal of this disk is inclined with respect to the beam propagation axis by the angle ϑ, the effective optical cross-section of the target amounts to

$$d_e = \sqrt{d_{cs} \cdot d_{cs,proj}} \quad (6)$$

with the projected disk diameter $d_{cs,proj} = d_{cs} \cos\vartheta$, cf. the drawing in Fig. 3, and $r_e = d_e/2$.

In laser ranging operations, the beam spot in orbit is typically significantly larger than the tracked object,

which is in usually a few meters in size while, as can be derived from Eq. 1, the spot extension exhibits at least several tens of meters. Hence, not only Gaussian beam propagation but as well diffraction has to be considered compute the reflected beam.

As an approximation for the propagation of the reflected beam, we consider diffraction effects separately from Gaussian propagation of the divergent laser beam. For the latter, we assume that beam cut-out from outshining the target yields a reduced beam radius which, using the cut-out ratio $q_w = r_e/w(z_1)$, leads to a glint radius of $w_G = q_w \cdot w(z_1 + z_2)$ on ground, discarding any diffraction effects. Here, z_2 is the distance between target at ground position of the glint.

On the other hand, for the computation of diffraction, we discard the beam divergence and assume instead that a plane wavefront arrives at the target. Particularly for small targets, the spot radius r_d of the laser glint on ground at the distance z_2 will then be significantly larger than the target itself. The radius r_d can be computed from the glint's intensity distribution $I(r)$ which, however, is non-Gaussian but exhibits several minima and maxima from interference. Therefore, we define r_d according to the energy that would correspond to a Gaussian beam radius by

$$\frac{\int_0^{r_d} I(r) \cdot r \, dr}{\int_0^{\infty} I(r) \cdot r \, dr} = 1 - e^{-2}. \tag{7}$$

The intensity distribution can directly be derived from the beam amplitude $A(r)$ via $I(r) = |A(r)|^2$ which is given by the Fresnel diffraction integral for a plane wavefront and a homogeneous intensity profile by [30]

$$A(x, y, z_2, r_e) = \frac{-i \exp(ikz_2)}{\lambda z_2} \tag{8}$$

$$\times \exp\left[\frac{ik}{2z_2}(x^2 + y^2)\right] \cdot \int_0^{2\pi} \int_0^{r_e} \exp\left(\frac{ik}{2z_2} r^2\right)$$

$$\cdot \exp\left[\frac{-ik}{z_2}(x \cdot r\cos\varphi + y \cdot r \sin\varphi)\right] \cdot r \, dr \, d\varphi$$

where $k = 2\pi/\lambda$ is the wavenumber.

Combining the considerations on divergence and diffraction we approximate the spot radius r_g of the laser glint on ground by the square sum of the beam radius from Gaussian propagation w_G, and the spot radius r_d due to diffraction by

$$r_g = \sqrt{w_G^2 + r_d^2}. \tag{9}$$

From this, the glint fluence Φ_g can be derived using the spot area on ground, $A_g = \pi r_g^2$, and the incident energy E_g given by

$$E_g = E_L \cdot (1 - E(\zeta)) \cdot q_e \cdot (1 - E(\zeta')) \tag{10}$$

where q_e denotes the energy fraction of the beam that is reflected at the target, which can be obtained from corresponding integration of the beam profile with radius r_e at z_1.

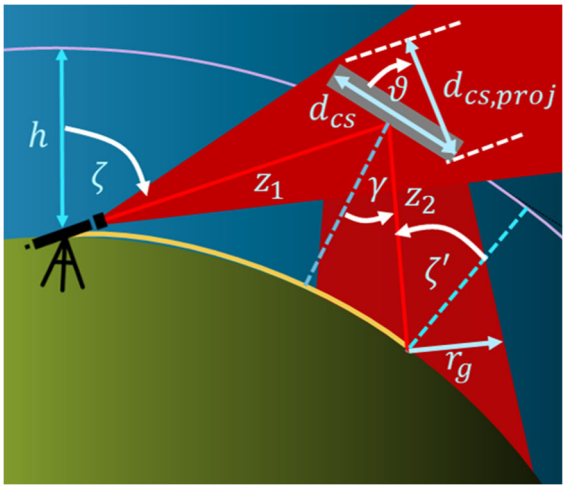

Figure 3. Schematics of laser beam propagation (not to scale).

3.4 Risk Assessment

For a quantitative risk analysis, we use an MPE-excess factor, defined as the ratio $q_{\Phi,1}$ of the maximum fluence within the glint to the applicable maximum permissible fluence, i.e., $q_{\Phi,1} = 2\,\Phi_g/\Phi_{MPE}$. Here, the factor of 2 refers to the consideration that in a Gaussian beam profile the maximum fluence is twice the average fluence.

Directly at the transmitter aperture of the laser ranging station, the MPE for a single laser pulse is exceeded for most of the outlined laser systems by two to four orders of magnitude, cf. Fig. 2. Only for UROL and SMIL $q_{\Phi,1}$ is slightly below 1. However, the excess factor for the thermally corrected single-pulse MPE exceeds 1 already after less than 0.1 seconds irradiation time due to the high pulse repetition rate. In contrast, for the "eye-safe" JKO2 the thermally corrected single pulse exposure stays well below the related MPE. Moreover, the MPE for accumulated pulses is not reached there before an overall irradiation time of at least 2 seconds has passed.

For the laser radiation reflected from a debris object, short propagation distances apparently are the most critical settings in the scenario shown in Fig. 3 since the beam radius increases with distance due to beam divergence, which, in turn lets the fluence decrease. Therefore, we start our assessment at $\zeta = \zeta' = 0°$, i.e., pointing to zenith with reflection back on the same path, which is illustrated for our laser ranging stations in Fig. 4.

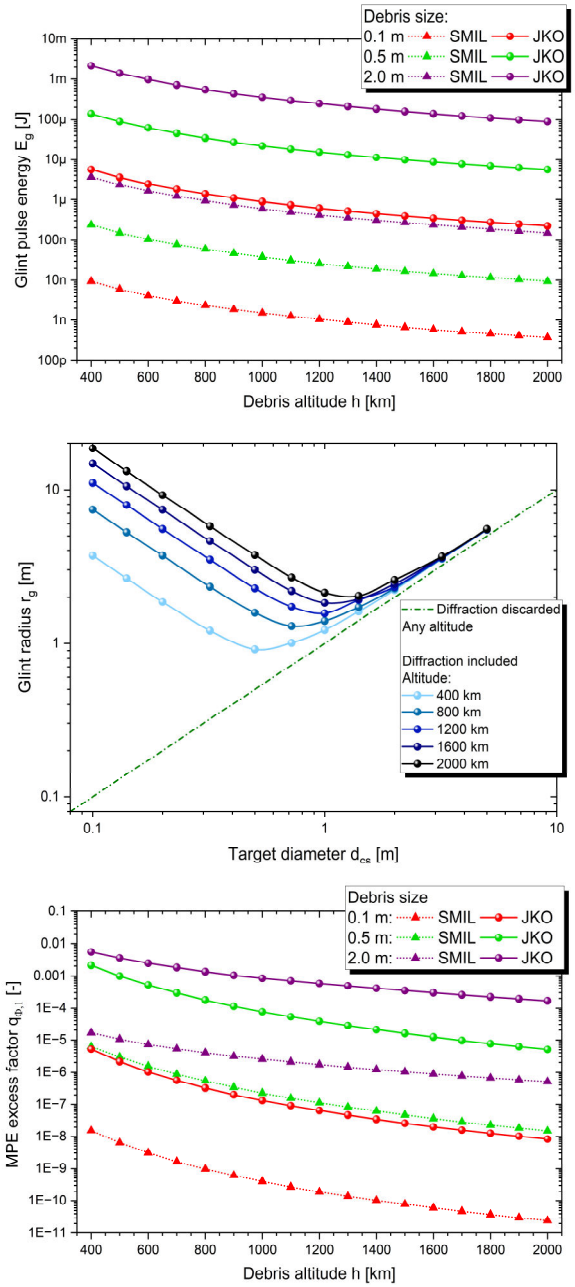

Figure 4. Glint pulse energy (top), radius (middle), and single-pulse MPE excess factor (bottom) for beam pointing to zenith and perpendicular back-reflection ($\zeta = \zeta' = 0°$) of a laser beam emitted from DLR Stuttgart's SLR and SDLR stations SMIL and JKO.

It can be seen from Fig. 4 (top) that for trackable targets the pulse energy can already be reduced by more than two orders of magnitude provided the object is rather small. Additionally, as the beam enlarges for great propagation distances due to divergence, the energy reflected from beam cut-out can amount more than one order of magnitude less at high LEO altitudes compared to the reflected energy at low altitudes.

Regarding the glint radius on ground it can be taken from Fig. 4 (middle) that diffraction effects become relevant for small targets of one-meter size and less. In particular with very small targets, the glint radius can exceed a value predicted discarding diffraction by up to two orders of magnitude.

Overall, it can be seen from Fig. 4 (bottom) that the glint's peak fluence on ground stays several orders of magnitude below the maximum permissible exposure, in particular for small objects and high altitudes. For the SMIL station, pulse energies are around three orders of magnitude lower than with JKO, which is reflected in the upper as well as in the lower part of Fig. 4, since rather similar MPEs apply for both systems.

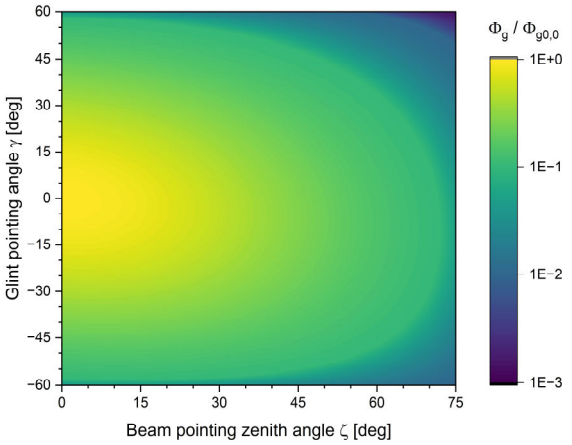

Figure 5. Ratio of glint fluence for slant beam paths with respect to the fluence for $\zeta = \gamma = 0°$. Target diameter: 0.5 m, altitude: 800 km.

With increasing beam pointing zenith angle ζ as well as with larger glint pointing angle γ, the MPE factor is furthermore reduced compared to the scenario with $\zeta = \gamma = 0°$, cf. Fig. 5. This stems from two different reasons: Firstly, the length of the absorption path through the atmosphere increases, diminishing the transmitted pulse energy. Secondly, the distance between target and laser station or observer, resp., enlarges which, for a greater z_1, reduces the amount of reflected pulse energy, and for a larger z_2, increases, due to beam divergence, the glint size on ground. The latter effects are particularly pronounced for targets at greater orbit altitudes.

Laser safety assessments have to be carried out for each system and its parameters specifically. As an exemplary computation, it can be seen from Fig. 6 that for GRZL systems, the MPE excess factors strongly deviate from the those of the DLR systems shown in Fig. 4 (bottom), since they significantly deviate from each other in terms of wavelength and transmitter aperture size (hence, regarding beam divergence, cf. Eq. 1) as well as concerning pulse energy and duration, cf. Fig. 2.

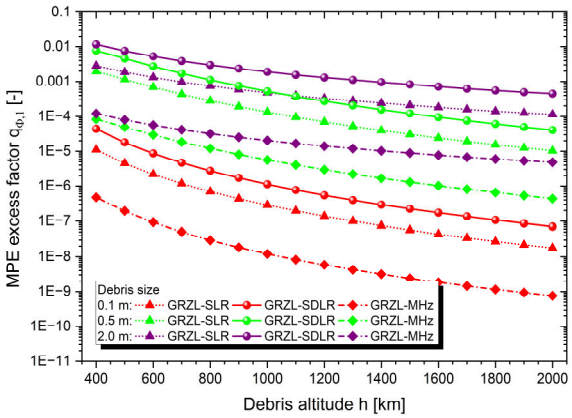

Figure 6. MPE excess factors for beam pointing to zenith and perpendicular back-reflection ($\zeta = \zeta' = 0°$) of a laser beam emitted from Graz (GRZL) laser ranging stations, cf. Tab. 1 and Tab. 2.

4 ORBITAL MOTION AND ROTATION

As high repetition rates are frequently employed in laser ranging, an observer might be endangered by a multitude of laser pulses. Different exposure limits apply in this case; therefore, the possible number of pulses has to be assessed.

4.1 Glint Motion

For this purpose, we firstly analyze how the glint position moves on ground, which yields an estimate for the applicable number of pulses $N_p \approx 2\, r_g\, f_{rep}/v_g$, where v_g is the velocity of the glint on ground. Hence, for a worst-case analysis, it is reasonable to compute the minimum glint velocity to derive the maximum conceivable number of pulses for a given laser exposure scenario.

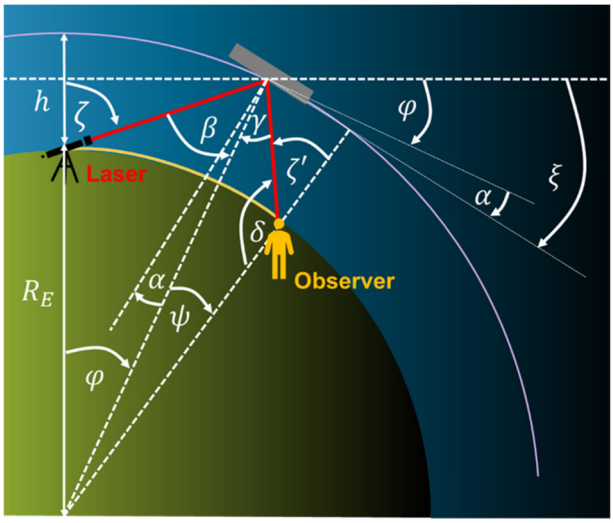

Figure 7. Observation geometry for specular reflection from rotating space debris on a circular orbit.

In general, the glint's motion is connected with the orbital motion where the target's rotation can either amplify, diminish or even reverse it, cf. the green and violet arrows shown in Fig. 1. For a quantitative assessment, the observation geometry has to be analysed in detail, cf. Fig. 7.

For our analysis, we assume a circular orbit, where the time-dependent position angle φ is given by

$$\varphi(t) = \varphi_0 + 2\pi\, t/T \qquad (11)$$

where the orbital period T amounts to

$$T = 2\pi\sqrt{(R_E + h)^3/GM} \qquad (12)$$

with the Earth's mean radius $R_E = 6367.5\ km$, gravitational constant G, and Earth's mass M yielding $GM = 398{,}600.4\ km^3/s^2$ [29].

Regarding the debris' rotation we assume that the rotational axis is perpendicular to the plane of projection in Fig. 7. The time-dependency of the debris orientation angle ξ is then

$$\xi(t) = \xi_0 + 2\pi\, t/T_D \qquad (13)$$

where T_D is the debris rotation period which might be derived from light curve analysis. It can be seen from Fig. 7 that a possible difference between φ and ξ, i.e., when the object's surface is not tangential to the circular orbit, results in a non-zero angle α between the debris nadir direction and its surface normal.

The zenith angle of the debris object is represented by ζ for the laser position and ζ' for the observer position, respectively. β denotes the angle between the incoming laser beam and the nadir direction of the debris object, while the angle between nadir and outgoing beam is given by γ.

From Fig. 7 it becomes obvious that the slowest ground motion of the glint can be expected at the nadir point of the object where the distance z_2 between glint and rotation axis is at its minimum, together with the related radial and orbital velocity of the glint's motion induced by the rotation of the debris. Note, however, that this estimate for motion in nadir cannot be generalized for all combinations of the debris' rotation and orbital motion since the debris' own orbital motion might partially compensate the abovementioned effects of glint rotation, which can be seen from Fig. 8.

For the considered geometry at the angular positions $\varphi = \psi = 0°$ with the initial orientations $\varphi_0 = \psi_0 = 0°$, the analytical estimate for the glint velocity,

$$v_g = 2(v_o \pm 2\pi\, t/T_D) \qquad (14)$$

can be derived from planar approximation of the Earth's surface, where v_o is the orbital velocity, "+" refers to

counter-clockwise (CCW) and "-" to clockwise (CW) debris rotation, respectively. As expected, very high ground velocities can be recorded for fast rotation while v_g becomes $2v_o$ for non-rotating objects.

For moderately high rotation periods, however, orbital motion and clockwise rotation partially compensate for each other and v_g drops even below v_o. Here, low glint velocities might imply the risk of exposure to a multitude of laser pulses, in particular around the minimum of $|v_g|$ at $T_D = 2\pi h/v_0$. Luckily, due to the curvature of Earth's surface, this is a transient minimum for $T_D = const.$ and v_g soon increases in the further course of the orbital motion.

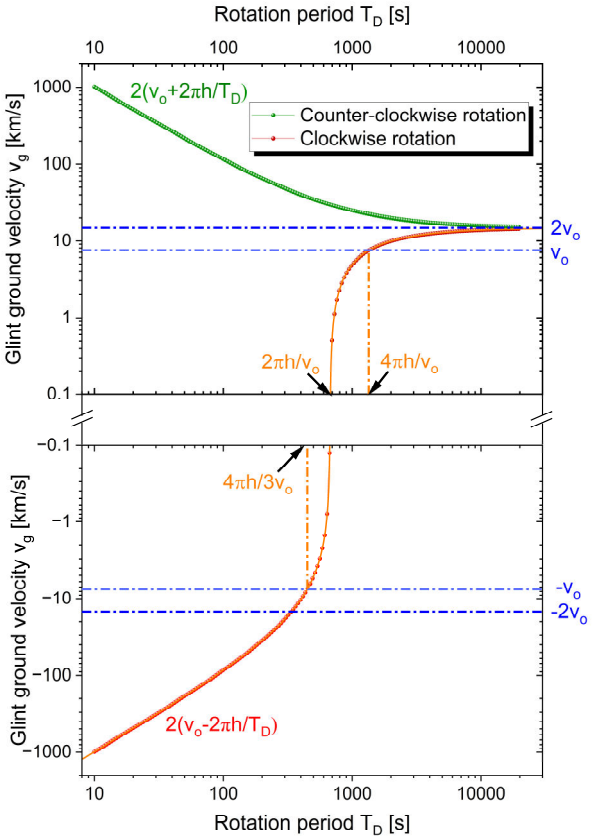

Figure 8. Numerical (symbols) and analytical (line) results for the glint velocity on ground from laser reflection at debris in 800 km altitude (circular orbit). The orbit-induced velocity component is increased for counter-clockwise rotation (green line, cf. Fig. 7 for orientation), lowered for slow clockwise rotation (red line) and inverted for fast clockwise rotation.

Obviously, the coincidence of orbital plane and debris rotation comprising an in-plane observer at rest is a strong two-dimensional simplification. However, it appears to be appropriate for a worst-case analysis as 3D effects like, e.g., an oblique rotation axis or the observer's off-plane motion, are likely to only reduce the interaction time between laser beam and observer.

Nevertheless, for a sound risk analysis, numerical computation of the glint trajectory and size history is inevitable, in particular, since the ground velocity itself is not directly decisive for risk assessment. Instead, the *apparent* glint velocity $v_a = v_g \cos\zeta'$ has to be used which describes the motion of the glint over the eye's pupil of the observer staring at the debris object.

4.2 Risk Assessment

Glint radius r_g and apparent glint velocity v_a depend strongly on debris size and irradiation geometry and, hence, can vary significantly during a laser ranging operation. Therefore, it is helpful to analyse the fundamental characteristics of how both parameters impact the laser exposure on ground. In this regard, the apparent glint velocity v_a can be employed to derive the number of pulses from the repetition rate and the spot radius r_g. To simplify the computation, we assume that spot size and energy do not change while the glint skims the observer's eye. This allows for the consideration of the relative motion of the observer through a static laser glint at the velocity $-v_a$.

For this purpose, a line intersecting the Gaussian spot through its center is defined with an equidistant series of N_{test} positions x_i exhibiting a position interval of $\Delta x = v_a/f_{rep}$, which represents the different positions of the eye during its relative motion through the glint. Moreover, for each value of N_{test} the series of positions is centred at the centre of the Gaussian spot to ensure a proper worst-case assessment.

From this, the accumulated fluence Φ_{acc} with

$$\Phi_{acc}(N_{test}) = \sum_{i=1}^{N_{test}} \Phi(x_i) \tag{15}$$

and the corresponding exposure time T_{acc} with

$$T_{acc}(N_{test}) = (N_{test} - 1)/f_{rep} \tag{16}$$

can be derived.

As the MPE threshold depends on the duration of exposure, the MPE excess factor cannot directly be obtained from the maximum of the accumulated fluence. Instead, the risk has to be assessed for each pulse series individually and we define the MPE excess factor $q_{\Phi,N}$ which is decisive for this scenario using the most hazardous pulse series by

$$q_{\Phi,N} = \max_{N_{test}} \frac{\Phi_{acc}(N_{test})}{\Phi_{MPE,N}[T_{acc}(N_{test})]} \tag{17}$$

for which it is sufficient to restrict the number of pulses for testing to $N_{test} \leq 4\, r_g/\Delta x$ which represents the twofold of the glint's Gaussian diameter.

Summarizing the dependencies of the cumulative MPE

excess factor $q_{\Phi,N}$ on glint velocity and size, laser-specific risk assessment charts can be derived which are shown for our laser systems in Fig. 9. It can be seen from the graphics that $q_{\Phi,N}$ gets large for low apparent glint velocities since many pulses can be acquired while $q_{\Phi,N}$ decreases when the glint size increases which stems from the decreasing fluence in that case. Moreover, at very high apparent glint velocities, only in single laser pulse fits into the transient exposure geometry, depending on the glint radius. Beyond this transition, indicated by the green lines in Fig. 9, only the MPE limit for single laser pulses has to be considered.

It is important to note here that the MPE excess charts shown in Fig. 9-12 are system-specific, i.e., relate to the unattenuated pulse energy of the laser system itself. For risk assessment in a laser ranging scenario, data have to be downscaled accordingly by E_g/E_L to represent the exposure by laser light reflected at the debris object.

For the thermally corrected maximum exposure to single pulses, the number of pulses N_p has to be involved to derive the MPE limit using $\Phi_{MPE,T} = \Phi_{MPE,1} \times N_p^{-0.25}$. However, the underlying norm refers to accidental irradiation in a setup where each pulse exhibits the same fluence which is not the case here, since the observer's eye travels through the Gaussian intensity profile of the laser glint. Therefore, we use an equivalent pulse number instead which is given by the ratio of accumulated fluence to the fluence in the glint center. With that, the MPE excess factor $q_{\Phi,T}$ for thermally corrected single pulse exposure limit is given in analogy to factor $q_{\Phi,N}$ by

$$q_{\Phi,T} = \max_{N_{test}} \frac{\Phi_c}{\Phi_{MPE,T}[N_{test}]} \tag{18}$$

where Φ_c is the fluence in the spot center.

In the related MPE risk assessment charts for our laser ranging systems, we summarized the applicable single pulse threshold by plotting the maximum of standard and thermally corrected threshold. The transition between standard and thermally corrected MPE excess can be seen from the corresponding graphics shown in Fig. 10. At large glint velocities, in particular for small glint sizes, only a single pulse of the skimming glint enters the eye's pupil. Therefore, the MPE excess factor does not depend on the glint velocity in the single pulse regime mentioned earlier, which is located above the green dash-dotted line in the graphics.

Slightly below this transition line, the MPE excess factor increases for decreasing glint velocity, which indicates that the thermal correction becomes more and more relevant for decreasing glint velocity. In particular, it can be noted for the JKO configuration that for very low glint velocities is eventually exceeded as indicated by the dash-dotted orange line where the MPE excess factor becomes greater than one.

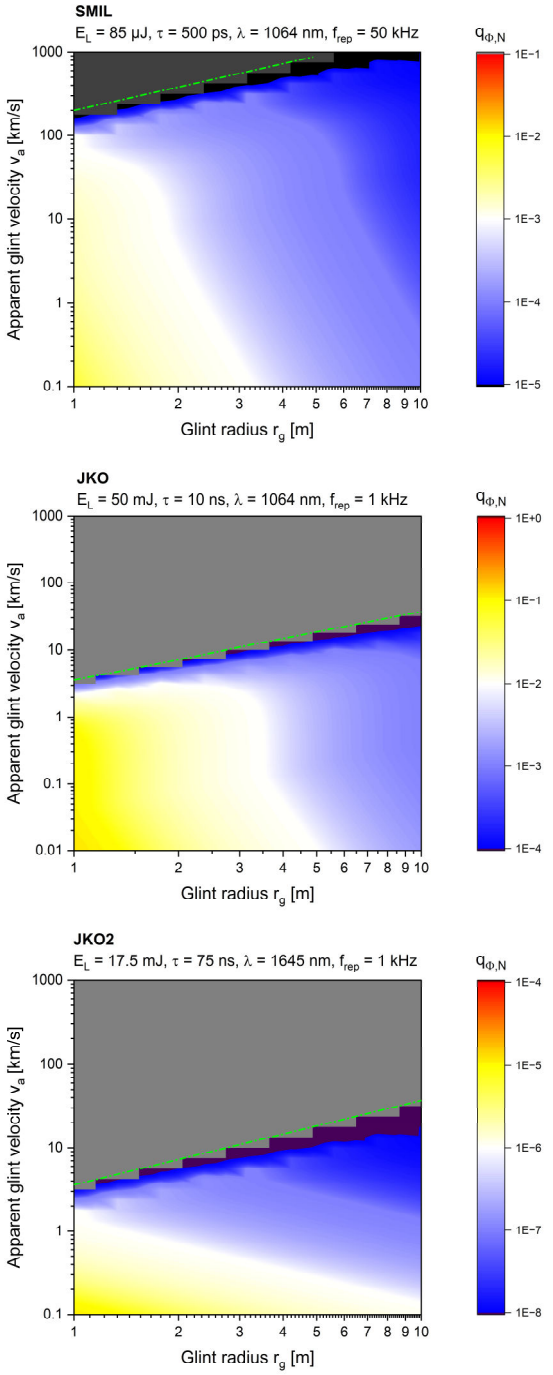

Figure 9. MPE excess charts of accumulated pulse energy from repetitive irradiation for DLR's near-infrared laser ranging systems: mini-SLR (top), Johannes-Kepler Observatory emitting at 1064 nm (middle) and 1645 nm (top), respectively. Results are computed for the unattenuated pulse energy of each system. For risk assessment, the results have to be downscaled by E_g/E_L.

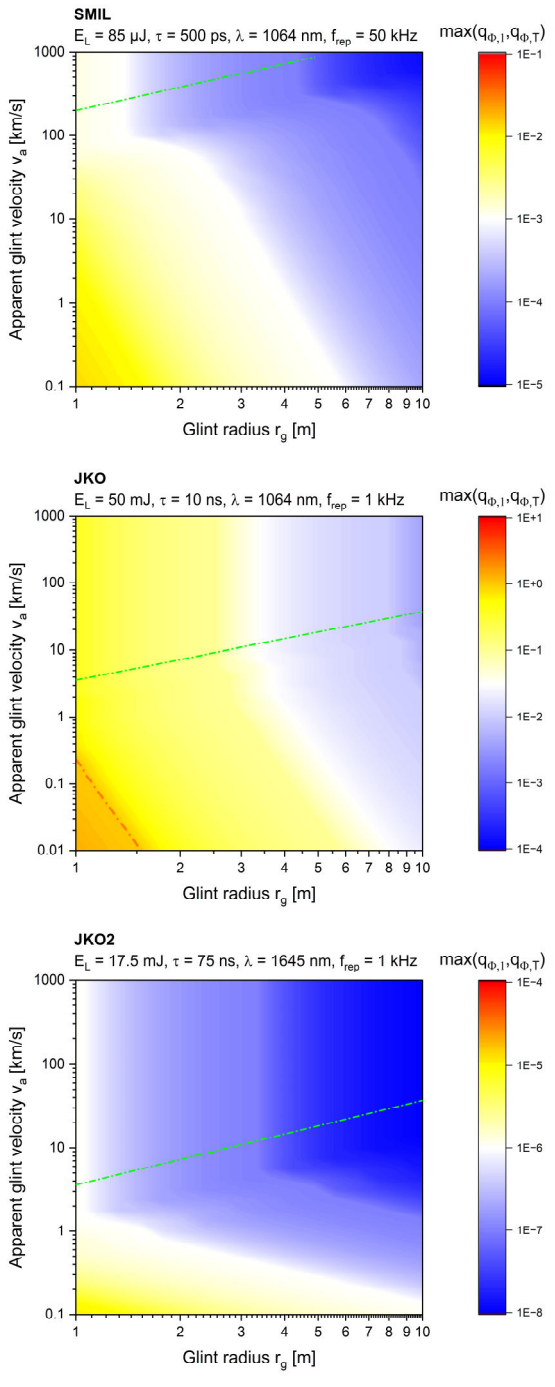

Figure 10. MPE excess charts of single pulse thresholds w/o thermal correction for repetitive irradiation for DLR's near-infrared laser ranging systems: mini-SLR (top), Johannes-Kepler Observatory emitting at 1064 nm (middle) and 1645 nm (bottom), respectively. Results are computed for the unattenuated pulse energy of each system. For risk assessment, the results have to be downscaled by E_g/E_L.

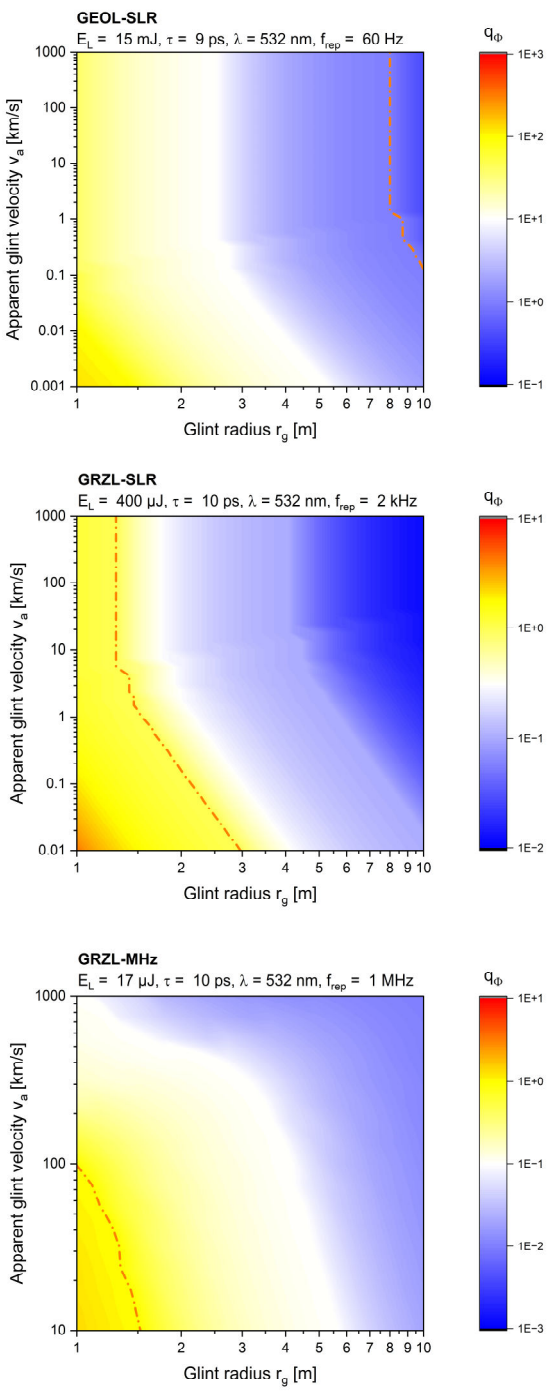

Figure 11. MPE excess charts regarding the minimum of all applicable MPE thresholds (i.e. the maximum MPE excess factor) for SLR systems with green light emitting lasers at pulse lengths in the picosecond regime: Geochang (top), Graz (middle), and Graz with MHz system (bottom, used as well for SDLR). Results are computed for the unattenuated pulse energy of each system. For risk assessment, the results have to be downscaled by E_g/E_L.

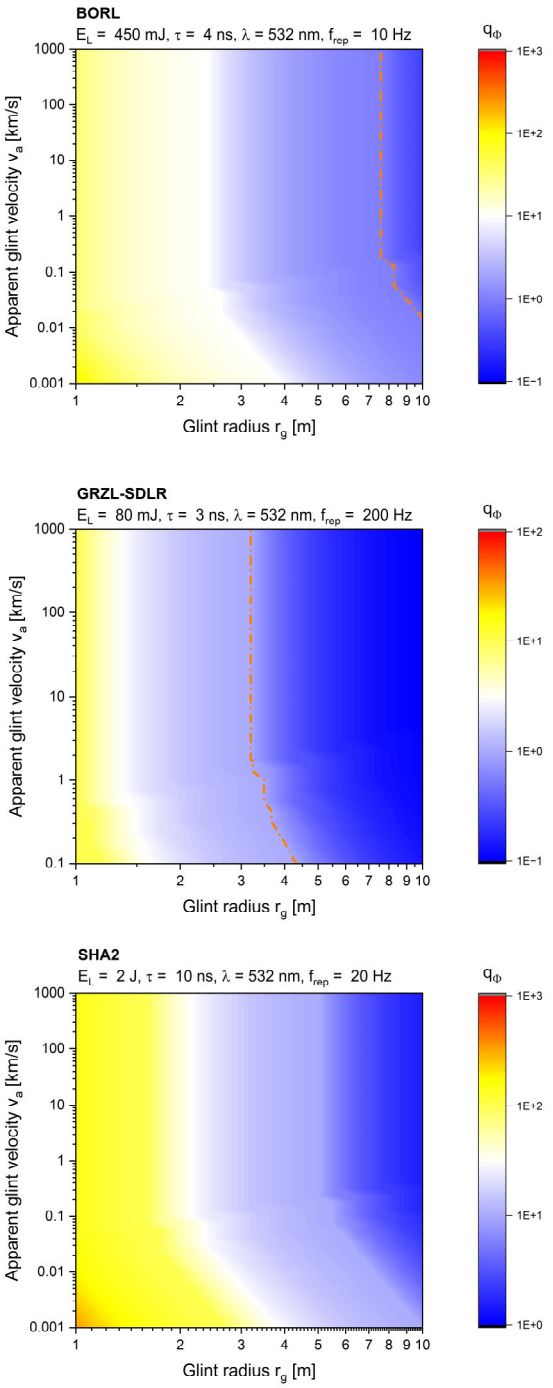

Figure 12. MPE excess charts regarding the minimum of all applicable MPE thresholds (i.e. the maximum MPE excess factor) for SDLR systems with green light emitting lasers at pulse lengths in the nanosecond regime: Borowiec (top), Graz (middle), and Shanghai (bottom). Results are computed for the unattenuated pulse energy of each system. For risk assessment, the results have to be downscaled by E_g/E_L.

At the end, the lowest of all three MPE thresholds applies for hazard assessment. In turn, the overall MPE excess factor q_Φ can be defined as

$$q_\Phi = \max\left(q_{\Phi,1}; q_{\Phi,N}; q_{\Phi,T}\right). \tag{19}$$

With this, risk assessment is laser ranging can be greatly facilitated, as the related *MPE excess charts*, cf. Fig. 11 and Fig. 12 for the other listed stations now summarize all fundamental quantities in a single graphics while not being constraint to any specific target or orbit. They enable extensive assessments, since effects of attenuation, overpass geometry or beam propagation are not involved here. Hence, the settings for a possibly harmful irradiation can strongly be constraint to combinations of v_a and r_g in which any of the three MPE thresholds might be exceeded.

As a general trend it can be seen in the MPE excess charts that systems using green light emitting lasers, in particular those with pulses in the picosecond regime, tend to operate closer to the MPE limits than the infrared-based systems shown in Fig. 9 and Fig. 10.

For the real-world use case, however, it has to be considered that these graphs have been computed for the system's unattenuated pulse energy. Considering losses by atmospheric attenuation and target outshining, the related MPE excess factors might in fact be a few orders of magnitude lower which decreases the range of possible hazardous glint velocities and radii. This, however, strongly depends on the irradiation geometry and has to be computed for each particular laser ranging maneuver in detail.

For all stations, the single pulse MPE becomes decisive while the MPE excess factor for pulse accumulation is relatively low.

5 DYNAMIC MPE STUDY

Departing from the parametric analysis within the concept of MPE excess charts we finally combine our considerations on beam propagation, diffraction, orbital and rotational motion with the MPE excess analysis to an overpass simulation for a specific target.

We assume a small (d_{cs} = 0.5 m) and a medium-sized (d_{cs} = 1 m) debris object at h = 1300 km and 550 km altitude, respectively, on a circular orbit. The target geometry is a modelled as a thin disk with perfectly flat and fully reflective surface. For the rotational motion, various periods are simulated, both clockwise and counter-clockwise. Moreover, phase offsets are set zero, i.e., $\varphi_0 = \xi_0 = 0°$. As laser source, the DLR station JKO is employed.

The temporal evolution of the MPE excess factor q_Φ for the glint on ground is shown in Fig. 13. It can directly be noted from comparison of the upper with the middle graph that orbit altitude and object size have a large impact on the MPE excess factor.

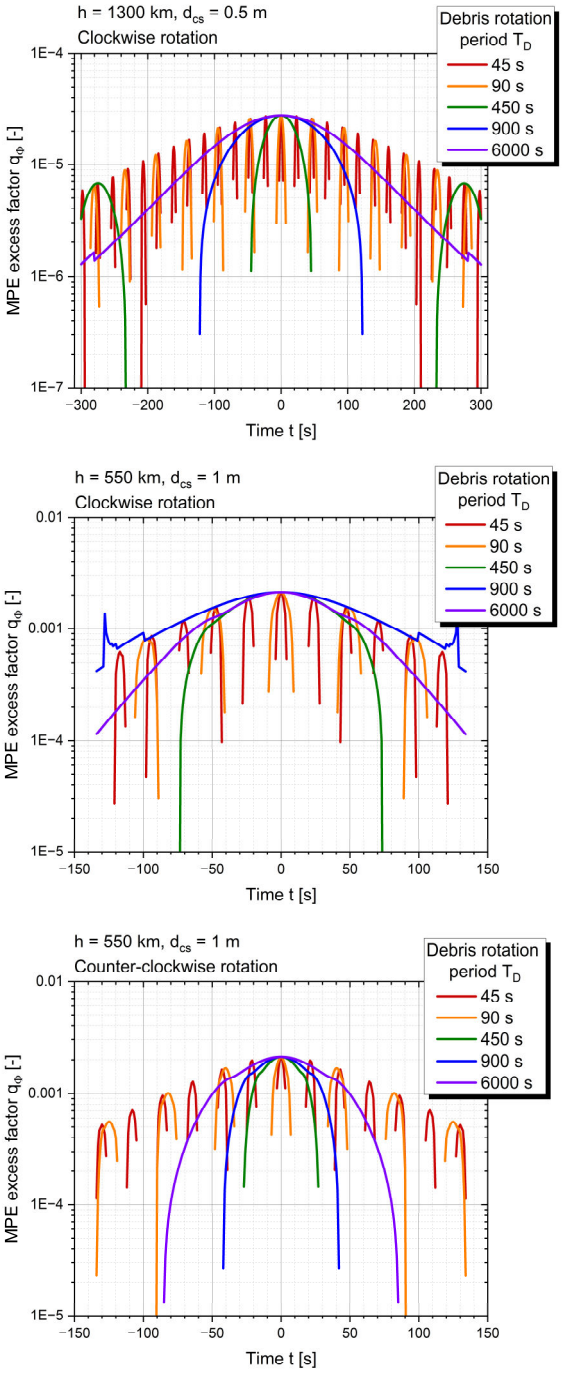

Figure 13. MPE excess factor for the laser glint on ground in laser ranging a flat, fully reflective object with JKO station: 0.5m-size object at 1300 km altitude rotating clockwise (top) in comparison with 1m-size object at 550 km altitude rotating clockwise (middle) and counter-clockwise (bottom), respectively.

For the large altitude of 1300 km, beam divergence greatly contributes to a large glint radius while diffraction effects even increase it further, which is significantly more pronounced for $d_{cs} = 0.5\,m$ than for $d_{cs} = 1\,m$. Moreover, significantly less laser pulse energy is reflected at the small target which eventually yields an MPE excess factor which is two orders of magnitude lower than in the case of the medium-sized target at 550 km altitude.

It can be seen from all three graphs that for short rotation periods, the temporal course of q_Φ comprises multiple peaks with steep ascent and descent around their center position. These peak maxima coincide with the points in time when the object is pointing into the nadir direction ($\psi = 0°$) and, hence, the glint velocity v_g and the glint radius r_g have their local minimum. Moreover, certain time intervals do not contain any data, which indicates that the reflected beam does not reach the ground at all but eventually escapes from LEO into space.

While the large glint velocity dominates for low rotation periods, the difference between clockwise and counter-clockwise rotation becomes pronounced for higher rotation periods. Comparing the upper with the middle graph of Fig. 13 it becomes evident that the rotational motion of the debris counteracts the glint motion on ground which comes from the debris' translational motion. Thus, the single peak in the middle MPE graph becomes significantly wider than the corresponding peak in the upper graph, where both rotation and translation yield glint motion components in the same direction.

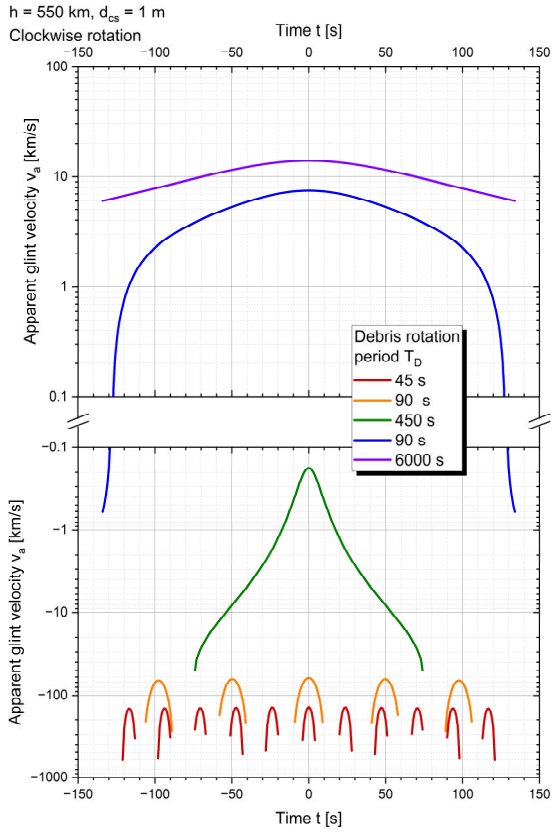

Figure 14. Apparent glint velocity for laser ranging of clockwise rotating debris at 550 km altitude.

From the analysis of the apparent glint velocity in the clockwise scenario, cf. Fig. 14, it can be seen that for the rotational periods 450 s and 900 s the glint becomes rather slow and v_a drops below 1 km/s. For 900 s it even changes its direction at $|t| \approx 128\,s$. Due to the related low glint velocities in the vicinity of this event, the MPE factor abruptly increases several times which demarcates that series of a few pulses are considered here by the thermally corrected MPE threshold.

Regarding the glint energy E_g it has to be remarked that the impact of oblique incidence is considerably large as the effective target cross-section is lowered then, yielding to larger outshining losses at the target, cf. Fig. 15 (top). In addition to that, the glint radius r_g strongly increases due to beam divergence when the direction of reflection largely deviates from the nadir direction, cf. Fig. 15 (bottom).

Combining glint velocity with glint radius, the simulation results can be represented as trajectories in the related MPE excess chart of the underlying laser ranging system, cf. Fig. 16, while the MPE excess factor itself has to be scaled via the ratio of glint energy to laser energy.

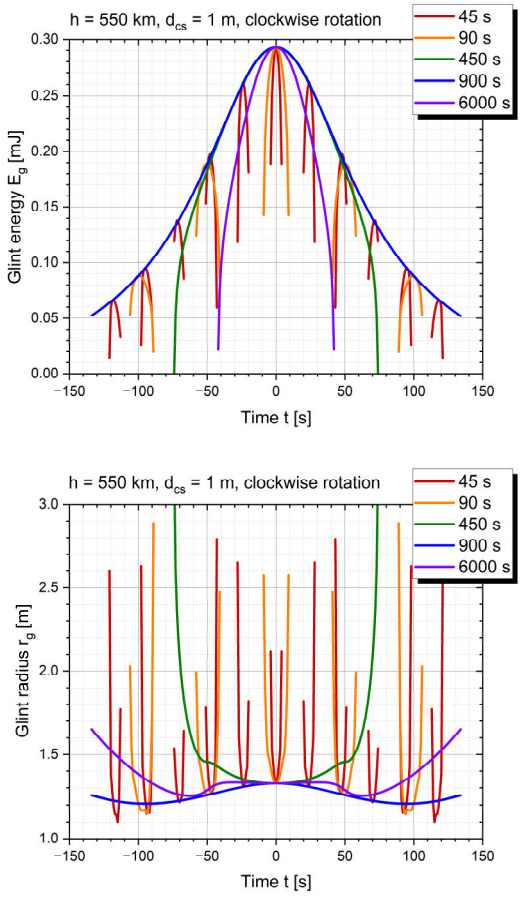

Figure 15. Glint energy (top) and radius (bottom) for laser ranging of clockwise rotating debris at 550 km altitude.

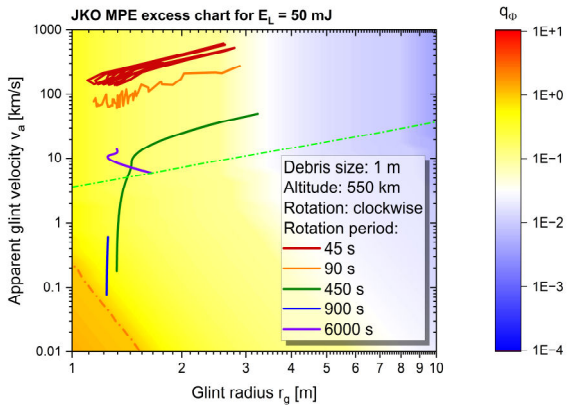

Figure 16. Glint parameter trajectories in the MPE excess chart of the employed laser ranging system. Clockwise rotating debris, 1 m size, at 550 km altitude. Note that for a quantitative assessment the MPE excess factor qΦ has to be scaled dynamically from the laser system energy (50 mJ) down to the actually applicable glint energy (0.05 – 0.3 mJ), cf. Fig. 15 (top).

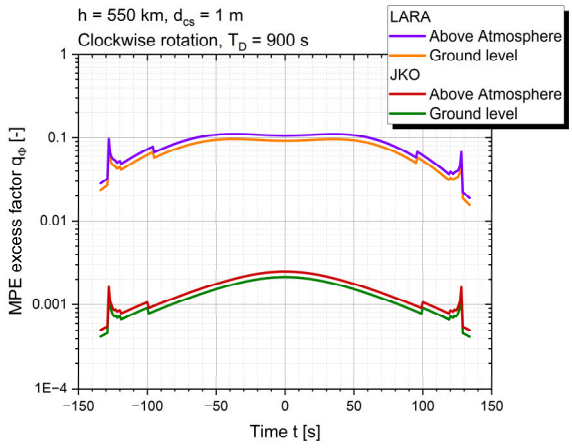

Figure 17. MPE excess factor for the laser glint on ground as well as above the atmosphere in laser ranging a flat, fully reflective object with a highly advanced ranging station in comparison to JKO station. LARA laser parameters equal those of JKO, albeit with a shorter pulse length (5 ns instead of 10 ns).

While all calculated fluences have been far below the MPE threshold in the shown study results, it has to be noted that highly advanced laser tracking systems might exhibit a larger risk potential. As an example, we have analysed a laser tracking concept that has been configured in order to support laser momentum transfer to space debris, denoted here as LARA. In that conceptual study, cf. [32], synergies of the laser tracking system with the high-power laser for momentum transfer are exploited. Hence, the tracking system can make use of a large transmitter aperture of D_T = 2.5 m in combination with an adaptive optics system for turbulence compensation. Moreover, the beam is focused

onto the targeted object yielding a spot size in orbit of only a few meters size, which greatly enlarges the amount of reflected laser pulse energy.

It can be seen from Fig. 17 that the risk for the LARA system is on the order of two magnitudes higher than for JKO. However, the laser exposure is still on an acceptable level, which applies as well for the results derived discarding atmospheric attenuation in downlink. In that scenario, which roughly represents the risk that is present at aircraft travel altitude, laser exposure is about 20% higher than on ground.

6 SUMMARY AND OUTLOOK

In our study, we have elaborated a method to assess potential risks from unintentional laser exposure stemming from reflections by space debris in laser ranging operations. For that purpose, we have introduced laser-specific MPE excess charts which allow to assess possible exceedance of legally applicable exposure thresholds in terms of glint velocity and glint radius.

MPE excess charts can be employed by analysing the ranging scenario regarding the emitted and reflected laser for which a methodology has been presented to incorporate a multitude of relevant effects comprising Gaussian laser beam propagation, atmospheric attenuation, target outshining, and diffraction.

The scenario has been simplified and reduced to a 2D geometry, while for a specific real-world use case the debris' rotational and orbital data would have to be used with an appropriate numerical propagator, including raytracing from station via debris to the glint's ground position.

It has to be noted here that these computations constitute as a worst-case assessment only using a perfectly flat surface while, depending on surface properties and target shape, a large fraction of laser light will likely not undergo specular reflection but be reflected diffusively, which again greatly reduces the related irradiation risk.

But even under those simplified worst-case assumptions we found that, at least for our DLR laser ranging station JKO, that is still enough margin to safely increase the laser pulse energy by up to two orders of magnitude in the investigated scenarios. Nevertheless, the picture might significantly change for laser operation in the visible and/or picosecond range, or, in general, for space debris which is observed from ground through a binocular during irradiation. In sum, this motivates our current research on eye-safe laser ranging at larger infrared wavelengths.

In general, our method might be helpful for applications using much higher laser power for, e.g., laser energy transmission or laser momentum transfer. In the field of laser ranging, however, it still might be worth considering the risks associated with accidently pointing a high-power laser for SDLR towards a large flat solar panel, which is easily conceivable at the background of the strongly increasing satellite constellation traffic. In this regard it would be helpful to experimentally investigate diffusive and specular reflection of a laser beam at such a surface in greater detail.

7 DISCLAIMER

This paper serves for orientation in laser risk assessment and methodology development only, without taking any liability for any harm caused by its real-world application. Instead, thorough laser risk assessment for the particular setup has to be carried out and responsibility for laser operations has to be taken by the assigned laser safety officer, cf. art. 4 para.2 in [2].

8 ACKNOWLEDGMENTS

The provision with institutional funding for this study is gratefully acknowledged by the authors.

9 REFERENCES

1. Steurer, J. et al. (2024). Algorithm for detecting airborne objects with a thermal infrared camera to ensure a safe operation of laser-optical ground stations. *Appl. Opt.* **63**(24), 6336-6344.

2. European Union (2006). Directive 2006/25/EC on the minimum health and safety requirements regarding the exposure of workers to risks arising from physical agents (artificial optical radiation). *Office Journal of the European Union* **L 114**, 38-59.

3. NASA (2013). International Laser Ranging Service. Online at *https://ilrs.gsfc.nasa.gov/about/index.html* (as of 12 February 2025)

4. Lim, H.-C. et al. (2018). Satellite Laser Ranging System at Geochang Station. *J. Astron. Space Sci.* **35**(4), 253-261.

5. Steindorfer, M.A. et al. (2025). Space debris and satellite laser ranging combined using a megahertz system, *Nat. Commun.* **16**(1), 575.

6. Hampf, D. et al. (2019). Satellite laser ranging at 100 kHz pulse repetition rate. *CEAS Space J.* **11**, 363-370.

7. Hampf, D. et al. (2024). The miniSLR: a low-budget, high-performance satellite laser ranging ground station, *J. Geodesy* **98**(8).

8. Kunimori, H. et al. (2000). Centimetre precision eye-safe satellite laser ranging using a Raman-shifted Nd:YAG laser and germanium photon counter, *J. Opt. A: Pure Appl. Opt.* **2**, 1-4.

9. Huber, C. et al. (2023). Transportable Station for Eye-Safe Laser Ranging of LEO Satellites and Space Debris. In: *Second International Orbital Debris Conference (IOC II)*, Paper 6064, Universities Space

Research Association, Lunar and Planetary Institute, Houston, USA.

10. Zhang, Z. et al. (2012). The use of laser ranging to measure space debris. *Res. Astron. Astrophys.* **12**, 212-218.

11. Lejba, P. et al. (2018). First laser measurements to space debris in Poland. *Adv. Space Res.* **61**(10), 2609-2616.

12. Wagner, G.A. et al. (2019). Mobile Station for Orbit Determination of Satellites and Space Debris. In: *First International Orbital Debris Conference (IOC 1)*, Paper 6203, Universities Space Research Association, Lunar and Planetary Institute, Houston, USA.

13. Steindorfer, M.A. et al. (2020). Daylight space debris laser ranging, *Nat. Commun.* **11**, 3735.

14. Degnan, J.J. (1993). Millimeter accuracy satellite laser ranging: a review. In *Contributions of Space Geodesy to Geodynamics: Technology* (Eds. Smith D.E. and Turcotte, D.L.), Geodynamics Series **25**, American Geophysical Union, pp133-162.

15. Dios, F. (2004). Scintillation and beam-wander analysis in an optical ground station-satellite uplink. *Appl. Opt.* **43**(19), 3866-3873.

16. Yura, H.T. (1973). Short-term average optical-beam spread in a turbulent medium. *J. Opt. Soc. Am.* **63**(5), 567-572.

17. Scharring, S. et al. (2021). LARAMOTIONS: a conceptual study on laser networks for near-term collision avoidance for space debris in the low Earth orbit. *Appl. Opt.* **60**(31), H24-H36.

18. Fante, R.L. (1975). Electromagnetic beam propagation in turbulent media. *Proc. IEEE* **63**(12), 1669-1692.

19. Canuet, L. (2014). *Atmospheric turbulence profile modelling for satellite-ground laser communication*. Universitat Politècnica de Catalunya.

20. McClatchey, R.A. et al. (1972). *Optical properties of the atmosphere*. Air Force Cambridge Research Laboratories.

21. Nussbaum, M. et al. (2022). Spectral Light Curve Simulation for Parameter Estimation from Space Debris. *Aerospace* **9**, 403.

22. Nicodemus, F.E. et al. (1977). Geometrical considerations and nomenclature for reflectance. *National Bureau of Standards Monograph* **160**, U.S. Department of Commerce.

23. Dana, K.J. et al. (1999). Reflectance and texture of real-world surfaces, *ACM T. Graphic.* **18**(1), 1-34.

24. Smith, W.A.P. & Hancock, E.R. (2009). A unified model of specular and diffuse reflectance for rough, glossy surfaces. In *2009 IEEE Conference on Computer Vision and Pattern Recognition*. IEEE Computer Society, Washington DC, USA, pp643-650.

25. Butler, S.D., Nauyoks, S.E. & Marciniak, M.A. (2015). Comparison of microfacet BRDF model elements to diffraction BRDF model elements. *Proc. SPIE* **9472**, 94720C.

26. Lu, M., Zhang, S. & Wang, Z. (2021). Establishment and verification of diffraction BRDF model for scratched material surface. *Opt. Laser Eng.* **142**, 106597.

27. Leader, J.C. (1979). Analysis and prediction of laser scattering from rough-surface materials. *J. Opt. Soc. Am.* **69**(4), 610-628.

28. Speiser, J. (2024). Unpublished data. Institute of Technical Physics, DLR Stuttgart, Germany.

29. Willison, A. & Bédard, D. (2015). Light Curve Simulation Using Spacecraft CAD Models and Empirical Material Spectral BRDFs. In *2015 AMOS Technical Conference Proceedings*. Maui Economic Development Board, Kihei, Hawaii, USA.

30. McKechnie, T.S. (2016). *General Theory of Light Propagation and Imaging Through the Atmosphere,* Springer, Cham, Switzerland, pp71-72.

31. Montenbruck O. (2011). Bahnmechnanik. In *Handbuch der Raumfahrttechnik* (Eds. Ley, W., Wittmann, K. & Hallmann, W.) Carl Hanser Verlag, Munich, Germany, pp74-101.

32. Cordelli, E. et al. (2021). Ground-based laser momentum transfer concept for debris collision avoidance. In *72nd International Astronautical Congress (IAC)*. Paper IAC-21-A6,6,2,x66062.